Extreme Mechanics Letters 1 (2014) 76–82

Contents lists available at ScienceDirect

Extreme Mechanics Letters

journal homepage: www.elsevier.com/locate/eml

Pattern morphology in the elastic sewing machine

Mohammad K. Jawed [a], Pedro M. Reis [a,b,*]

[a] Department of Mechanical Engineering, Massachusetts Institute of Technology, Cambridge, MA 02139, United States
[b] Department of Civil & Environmental Engineering, Massachusetts Institute of Technology, Cambridge, MA 02139, United States

ARTICLE INFO

Article history:
Received 13 November 2014
Received in revised form 4 December 2014
Accepted 4 December 2014
Available online 9 December 2014

Keywords:
Thin elastic rods
Nonlinear geometry
Pattern formation

ABSTRACT

We present results from a numerical investigation of the coiling patterns obtained when a slender elastic rod is deployed onto a moving substrate. The Discrete Elastic Rods method is employed to explore the parameter space, construct phase diagrams, identify their phase boundaries and characterize the pattern morphology. The various length scales of the patterns are primarily set by the gravity-bending length and depend only logarithmically on the deployment height. The curvature near the contact point, together with the dimensionless speed mismatch between deployment and the belt, dictate the characteristics of the patterns. The phase boundaries are found to be independent of both the gravito-bending length and the deployment height, as long as the latter is above a threshold value. We also evaluate the relative importance of twist and curvature strains, which confirms that bending has a dominant role.

1. Introduction

Deployment of a slender filament onto a rigid substrate is a scenario that arises in a variety of engineering applications. From the micron to the kilometer, examples include carbon nanotube serpentines [1], electrospinning of polystyrene fibers [2], 3D-printing [3], stretchable electronics components [4] and transoceanic cables [5]. As the filament impacts the substrate (static or moving) the coiling of the filament can lead to complex patterns.

When the filament is a viscous thread, these periodic coiling patterns resemble the stitches of a sewing machine and the process has come to be known as the 'fluid mechanical sewing machine' (FMSM) [6]. Even when the substrate is static, the fluid coils in a nearly circular patterns with a radius dictated by the competition between viscous, gravitational, and inertial effects. This coiling problem, known as the 'liquid rope trick', has been studied through experiments and scaling analyses [7–9], and three distinct coiling regimes (viscous, gravitational, and inertial) have been identified [10]. The buckling instability of liquid threads, upon which coiling ensues, has also been studied theoretically [11,12]. The problem has also been addressed numerically by solving a nonlinear boundary value problem [13], and regions of multistability have been reported [14]. In the FMSM, the rotational symmetry of the coiling instability is broken by the translation of the substrate, leading to a multitude of complex patterns. These patterns were first reported in experiments [6], and later rationalized by a stability analysis to predict the onset of the nonlinear modes [15]. The transitions between the various patterns as well as their frequency structure have been experimentally determined [16,17]. A numerical framework has been developed [18,19] using tools from discrete differential geometry [20] that is able to predictively simulate the patterns of the FMSM. A numerical description of the patterns, classified based on the Fourier spectra of the motion of the point of contact between the substrate and the thread, has also been studied in detail [21].

An analogy between the coiling of viscous threads and elastic ropes was first mentioned in 1958 [22] but a formal

* Correspondence to: MIT, 1-330, 77 Massachusetts Avenue, Cambridge, MA 02139, United States.
E-mail address: preis@mit.edu (P.M. Reis).

http://dx.doi.org/10.1016/j.eml.2014.12.004
2352-4316/

account for these similarities was only recently considered [23]. Indeed, when the filament is a thin elastic rod that impacts a rigid substrate, the coiling patterns are similar to that of the FMSM [24–27], such that the problem is now referred to as the 'elastic sewing machine' (ESM) [26]. The first numerical solution to coiling of flexible rods on a static substrate [24], however, involved a sign error in the inertial terms [25]. The system was later characterized experimentally, and compared against numerical solutions [25]. Similarly to the case of fluid coiling, three distinct coiling regimes were observed for elastic coiling (inertial, elastic, and gravitational). A moving substrate in the elastic case has been addressed experimentally and numerically, and a multitude of patterns were reported [26]. Despite these recent advances in the study of the ESM, a quantitative characterization and subsequent rationalization of all of the possible nonlinear patterns, in terms of the relevant physical and geometric parameters, remains an open topic.

We have recently studied the ESM [27] by combining precision desktop experiments with Discrete Elastic Rods (DER) simulations; a cutting edge computational tool ported from the Computer Graphics (CG) community [28,18]. These simulations have been accurately validated against experiments, with no fitting parameters [27]. The primary control parameters were identified to be the speed mismatch between the deployment and belt speeds, the gravito-bending length (the characteristic length scale of the problem) and the height of deployment. The specific cases of coiling onto a static substrate and the first sinusoidal mode on a moving substrate were studied in detail [27], but a quantitative characterization of the other nonlinear patterns has not yet been performed.

Here, we leverage the experimentally validated DER simulation tool to study all of the coiling patterns of the ESM. We perform a systematic numerical investigation and provide a description of the patterns morphology versus the physical and geometrical parameters of the system. Upon identification of the relevant length scales, we construct phase diagrams and identify their phase boundaries. The onset of coiling is first studied by analyzing the planar weakly nonlinear shapes of a rod held between the injector and the substrate. Moreover, we relate the physical parameters to the curvature of the rod near its contact point with the substrate. Particular emphasis is placed on the patterns that exhibit coiling loops and their wavelength is found to vary continuously across the phase boundaries. We quantify the relative importance of bending and twisting energies, which further emphasizes the importance of curvature near the contact point for pattern selection.

2. Problem definition

In Fig. 1A, we present a schematic of our problem. A thin elastic rod is deployed vertically from a height, H, and at a speed v, onto a rigid substrate (conveyor belt) that translates horizontally at speed, v_b. The control parameter of the system is taken to be the dimensionless speed mismatch, $\epsilon = (v - v_b)/v$, between the injector and the belt. The contact point between the suspended heel and the belt moves in the x–y plane, and 'prints' geometrically

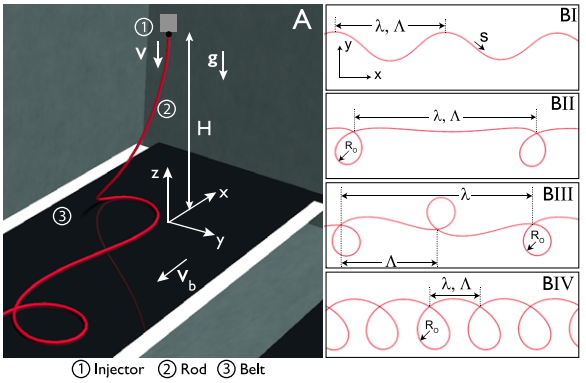

Fig. 1. (A) An injector (1) deploys a thin elastic rod (2) onto a conveyor belt (3). (B) Representative snapshots of the trace of the rod (L_{gb} = 3.3 cm and $\bar{H}$ = 15) left on the belt for the various coiling regimes: (I) Meandering, ϵ = 0.13; (II) Stretched coiling, ϵ = 0.33; (III) Alternating loops, ϵ = 0.5; (IV) Translated coiling, ϵ = 0.7. Definitions of the wavelength, λ, characteristic length, Λ, and loop radius, R_o, of the coiling patterns are also shown in schematic.

nonlinear patterns on the belt (see Fig. 1B): sinusoidal meandering (I), stretched coiling (II), alternating loops (III), and translated coiling (IV). More details of this setup were provided in [27].

The rod is assumed to be naturally straight and made out of an isotropic, linear elastic and incompressible material (Poison's ratio ν = 0.5), with Young's modulus, E, and shear modulus, $G = E/3$. The three contributions to the energy per unit length in the deformed rod are elastic, $\mathcal{E}_e$, gravitational, $\mathcal{E}_g$, and inertial, $\mathcal{E}_i$. We focus on a regime where v is low enough, so that inertia can be neglected. The elastic energy can have bending and twisting components, $\mathcal{E}_e = \mathcal{E}_b + \mathcal{E}_t$, but for the purposes of the present scaling description we ignore $\mathcal{E}_t$ (even it is included in the simulations, see Section 3). Taking the rod as inextensible (reasonable approximation given its slenderness) and balancing the gravitational and bending contributions, $\mathcal{E}_g \sim \mathcal{E}_e$, yields the gravito-bending length $L_{gb} = [(r_0^2 E)/(8\rho g)]^{1/3}$ [29,27], the primary characteristic length scale of our system. The deployment height, H, is the secondary length scale. Hereafter, we present all the lengths normalized by L_{gb} as denoted by an overbar, *e.g.* $\bar{\lambda} = \lambda/L_{gb}$.

3. Numerical experiments

Our numerical investigation makes use of the Discrete Elastic Rods (DER) method [28], which was previously validated against experiments with excellent agreement and no fitting parameters [27]. The source code is available for download in [30]. DER follows a Kirchhoff-like dynamic representation of an extensible rod [31], but starts from a discretized version of the elastic energy functional and subsequently follows an approach from discrete differential geometry [20] to derive the corresponding equations of motion. This approach has the benefit of capturing important features of the underlying nonlinear geometry, which are often lost in more standard discretization methods for the well established smooth equations [32].

The rod is described by its arc-length parameterized centerline, $\boldsymbol{\gamma}(s)$, and a material frame represented by the

angular deviation, $\theta(s)$, from the reference frame, which is maintained across time steps using parallel transport. Stretching and bending are captured by the deformation of the centerline, while twisting is described by the rotation of the material frame. The twist and curvature of the deformed configuration are given by $\theta'(s)$ and $\kappa(s) = |\boldsymbol{\gamma}''(s)|$, respectively, where prime refers to differentiation with respect to s.

The contact between the rod and the substrate is modeled by Dirichlet boundary conditions (pinned nodes) that prevent translation after deposition. However, the edges of the deposited rod (an edge connects two consecutive nodes) that lie within an arc-length αL_{gb} from the contact point, are allowed to rotate about the centerline of the rod. We have found that our quantities of interest (*e.g.* coiling radius and pattern wavelength) are insensitive to α in the range $5 \leq \alpha \leq 50$, so we chose $\alpha = 5$.

Our numerical exploration involves systematic sweeps along ϵ and $\bar{H}$ for rods with different values of L_{gb}. Unless stated otherwise, the geometric and material parameters of our *representative* rod are (identical to the experiments in [27]): $r_0 = 0.16$ cm, $\rho = 1.18$ g/cm^3, and $E = 1.3$ MPa (*i.e.* $L_{gb} = 3.3$ cm), deployed from $\bar{H} = 15$ at $v = 1.0$ cm/s. For sweeps along the range $0 \leq \epsilon \leq 1$, we start with a belt speed of $v_b = 1.0$ (or 0) cm/s and step up (or down) along ϵ by decreasing (or increasing) the belt speed in increments of 0.01 cm/s, while keeping the injection speed fixed. Steady patterns are ensured by injecting at least $500L_{gb}$ length of rod onto the belt. The inherent multistability [27] requires a bidirectional sweep, along both $\epsilon = 0 \rightarrow 1$ and $\epsilon = 1 \rightarrow 0$.

Throughout, the gravito-bending length is varied (when not kept fixed at the *representative* case of $L_{gb} = 3.3$ cm) in the range $1.0 < L_{gb}$ (cm) < 10.0, by fixing two of the three parameters (r_0, ρ, E) and varying the third by up to three orders of magnitude. The ranges explored are: $0.07 < r_0$ (cm) < 0.6, $0.05 < E$ (MPa) < 30, and $0.05 < \rho$ (g/cm^3) < 25. The dimensionless deployment height (when not kept fixed at the *representative* case of $\bar{H} = 15$) is varied by fixing $L_{gb} = 3.3$ cm and changing H.

4. Pattern selection

In Figs. 2A and B, we present phase diagrams in the (L_{gb}, ϵ) and $(\bar{H}, \epsilon)$ parameter spaces, fixing $\bar{H} = 15$ and $L_{gb} = 3.3$ cm, respectively. The data points correspond to the phase boundaries between consecutive patterns, with open (or filled) symbols obtained for $\epsilon = 0 \rightarrow 1$ (or $\epsilon = 1 \rightarrow 0$). Three patterns are observed when increasing ϵ: meandering (Fig. 1B,I), alternating loops (Fig. 1B,III), and translated coiling (Fig. 1B,IV). Along the reverse sweep ($\epsilon = 1 \rightarrow 0$), an additional stretched coiling pattern (Fig. 1B,II) is obtained. There are extended regions of bistability, *e.g.* (I,II), (I,III) and (III,IV). Note that in [27] we reported phase diagrams with these same patterns but did not systematically explore their dependence on L_{gb} nor $\bar{H}$.

Since the (L_{gb}, ϵ) phase boundaries in Fig. 2A are vertical (solid lines), we conclude that the pattern selection is independent of L_{gb}. The numerical values of the location of the phase boundaries, ϵ_t^i, are provided in Table 1, where i is the label for the respective boundaries: I–(I,II), (I,II)–(I,III), (I,III)–III, III–(III,IV) and (III,IV)–IV. From Fig. 2B, we also conclude that the $(\bar{H}, \epsilon)$ phase boundaries are independent of the deployment height, with some deviations in the I–(I,II) and (I,III)–III boundaries that are only constant for $\bar{H} > 9.65$ and $\bar{H} > 30.02$, respectively. For the other boundaries, (I,II)–(I,III), III–(III,IV) and (III,IV)–IV, the variation in ϵ_t^i is less than 10% in the range $3.0 < \bar{H} < 100$.

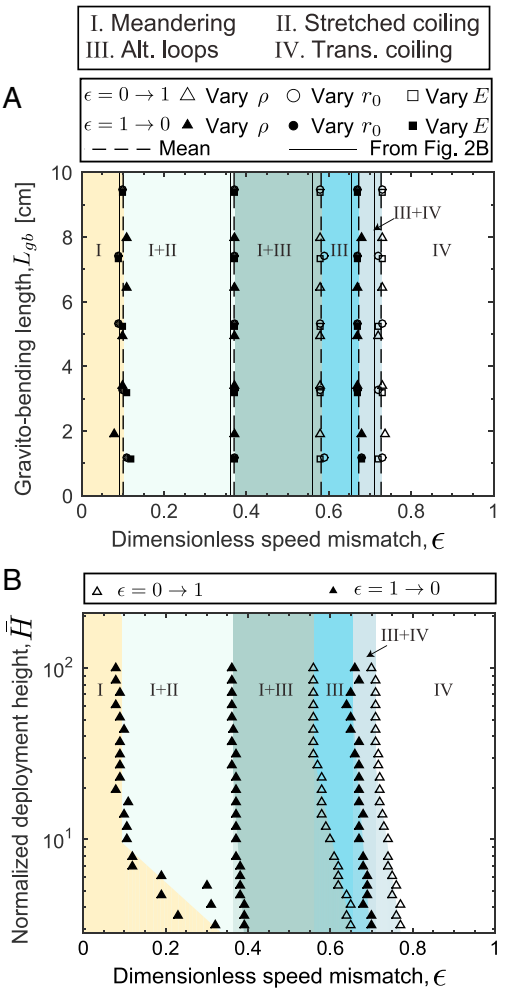

Fig. 2. Phase diagrams of the (A) parameter space (L_{gb}, ϵ) with normalized deployment height fixed at $\bar{H} = 15$, and (B) parameter space $(\bar{H}, \epsilon)$ with $L_{gb} = 3.3$ cm. The data-points correspond to the dimensionless speed mismatch, ϵ, at the transition between two states. Open symbols represent the phase transitions along $\epsilon = 0 \rightarrow 1$, whereas filled symbols stand for the transitions along $\epsilon = 1 \rightarrow 0$.

Table 1
Numerical values of dimensionless speed mismatch, ϵ_t^i, at the phase boundaries shown in Fig. 2.

Boundary	ϵ_t^i
I–(I,II)	0.09 ± 0.02
(I,II)–(I,III)	0.37 ± 0.00
(I,III)–III	0.56 ± 0.00
III–(III,IV)	0.67 ± 0.01
(III,IV)–IV	0.73 ± 0.01

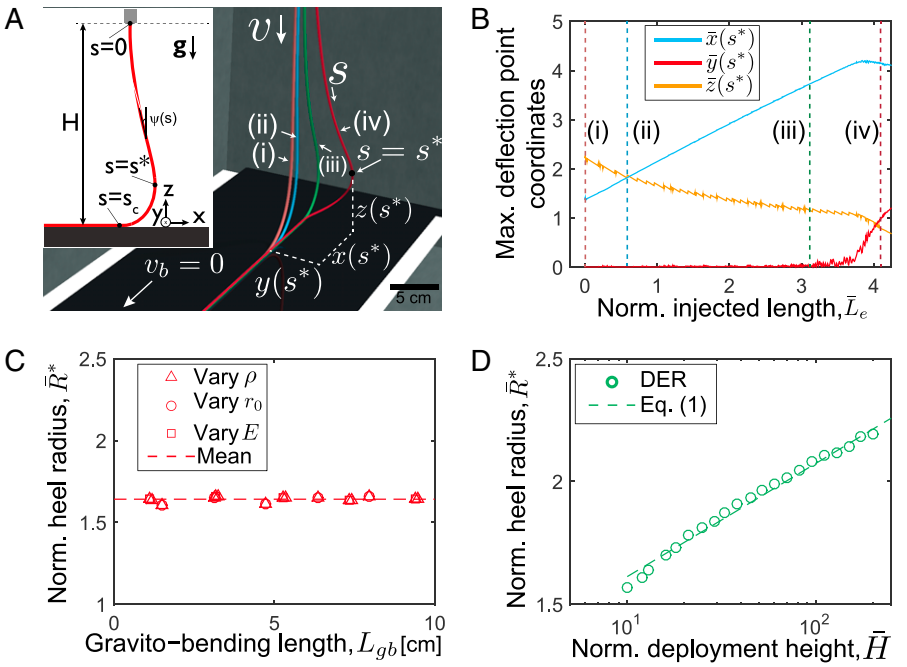

Fig. 3. (A) Three dimensional perspective of the suspended heel at normalized injected length of (i) $\bar{L}_e = 0$, (ii) $\bar{L}_e = 0.6$, (iii) $\bar{L}_e = 3.2$, and (iv) $\bar{L}_e = 4.2$. In (iv), the deformation is non-planar with non-zero $y(s^*)$. Inset: schematic diagram of the projection of the suspended heel onto the x–z plane. (B) Coordinates of maximum deflection point, (x, y, z), at $s = s^*$ as function of the normalized extra length, $\bar{L}_e$. The vertical dashed lines correspond to the configurations presented in (A). (C) Heel radius, R^*, as a function of the gravito-bending length, L_{gb}, when deployed from a height of $\bar{H} = 15$. (D) Variation in R^* with normalized deployment height, $\bar{H}$, for a rod with $L_{gb} = 3.3$ cm. The dashed line is the fit of the data to Eq. (1), with $D_1^* = 0.20 \pm 0.01$ and $\beta^* = 1.15 \pm 0.05$.

The reason for this deviation from height-independent behavior is that, when $\bar{H}$ is small, the bending energy of the rod dominates over its gravitational potential. The gravito-bending description mentioned in Section 2 is only valid for sufficiently large deployment heights.

5. Shape of the suspended heel

Previously, we had established a link between the shape of the suspended heel near the contact point and the morphology of the meandering patterns [27], remaining, however, at the level of scalings. We proceed with a more comprehensive characterization of the shape of the heel near the belt, as a function of the geometric and material parameters (L_{gb} and $\bar{H}$) using the following protocol. We first initiate the simulations by deploying the rod onto the belt with $\epsilon = 0$ ($v = v_b$) so that the segment of rod between the injector and the substrate (the suspended heel) assumes a x–z planar catenary configuration; see Fig. 3A(i). The belt is then switched off ($v_b = 0$ cm/s) at $t = t_i$ while keeping the injection speed unchanged. This results in the gradual accumulation of *extra length* of rod, $L_e(t) = \int_{t_i}^{t} v\, dt^*$, which increases the curvature near the contact point and eventually causes the planar catenary to buckle out of the x–z plane; see Fig. 3A(ii–iv).

Fig. 3B plots the coordinates of the maximum deflection point of the heel, $[x(s^*), y(s^*), z(s^*)]$, versus the normalized injected extra length, $\bar{L}_e$. The transverse coordinate remains $y(s^*) \sim 0$ until $\bar{L}_e \approx 3.5$; *e.g.* configurations (i) and (ii), in Fig. 3A. Beyond this point, there is out-of-plane deformation and $y(s^*) > 0$; *e.g.* configurations (iii) and (iv) in Fig. 3A.

Note that $x(s^*) \sim z(s^*)$ when $\bar{L}_e \approx 0.6$ (Fig. 3A,ii). When this happens, the segment of rod between the point of maximum deflection and the contact point with the belt can be approximated by a quarter circle with radius $\bar{R}^*$, the *heel radius*, which we regard as a shape parameter that we now quantify. The normalized heel radius is found to be constant, $\bar{R}^* = 1.64 \pm 0.01$, as a function of L_{gb} (Fig. 3C). Moreover, the dependence of $\bar{R}^*$ on $\bar{H}$ (Fig. 3D), is well described by

$$\bar{R}^* = D_1^* \log\left(\bar{H}\right) + \beta^*, \tag{1}$$

where $D_1^* = 0.20 \pm 0.01$ and $\beta^* = 1.15 \pm 0.05$ are numerical constants obtained by fitting the data. A similar logarithmic dependence on $\bar{H}$ was also found in [27], for the characteristic wavelength of the meandering patterns. This was rationalized by noting that the shape of the suspended heel above the point of maximum deflection, as measured by the angle ψ (see Fig. 3A, inset), scales as $\psi \sim (s^* - s)^{-1}$ and the logarithm dependence is obtained upon the integration $x(s^*) \sim \int_0^{s^*} \psi(s) ds$, which was required for the derivation of the onset wavelength. Moreover, comparing our results for $\bar{R}^*$ and those in [27] for the amplitude, A, of the meandering pattern mode reveals that $A \approx 2R^*\sqrt{\epsilon}$.

The linearity between R^* and L_{gb} and the logarithmic dependence of R^* on $\bar{H}$ will also be found for the length scales of all of the other coiling patterns analyzed next.

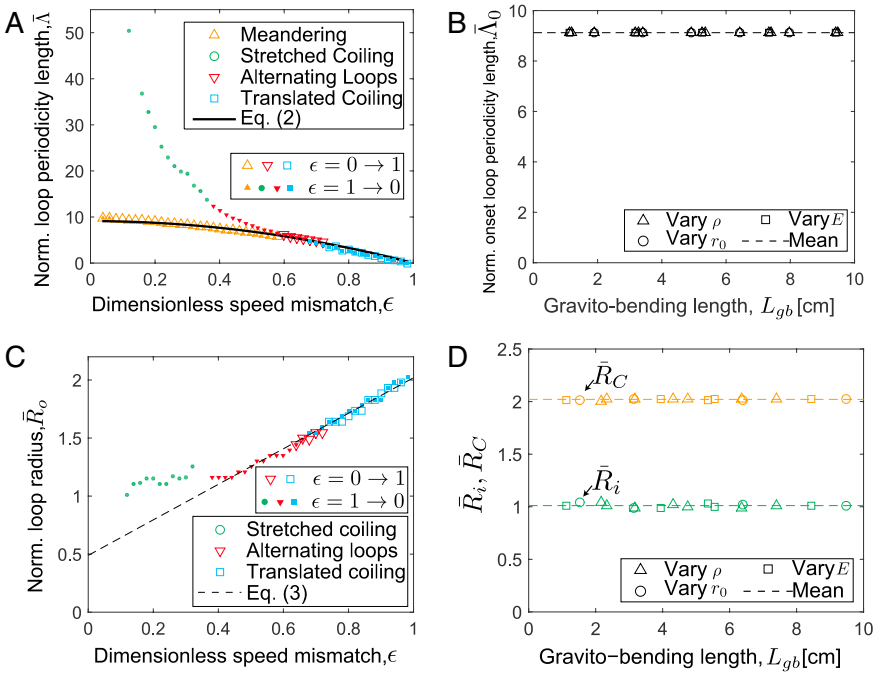

Fig. 4. (A) Normalized loop periodicity length, $\bar{\Lambda}$, as a function of the dimensionless speed mismatch, ϵ. (B) Variation in normalized onset loop periodicity length, $\bar{\Lambda}_0$, with the gravito-bending length, L_{gb}. (C) Normalized loop radius, $\bar{R}_o$, as a function of the dimensionless speed mismatch, ϵ. (D) Variation in the static coiling radius, $\bar{R}_C$, and onset radius, $\bar{R}_i$, with the gravito-bending length, L_{gb}. In (C) and (D), the open and filled symbols correspond to sweeps along the $\epsilon = 0 \rightarrow 1$ and $\epsilon = 1 \rightarrow 0$ directions, respectively.

6. Morphology of coiling patterns with loops

We turn to a systematic quantification of the morphology of all the patterns in Figs. 1 and 2 that form coiling loops (the meandering patterns were already analyzed in [27]). Our goal is to determine how the various features of these patterns (*e.g.* periodicity length scales and radius of the coiling loops) depend on the physical and control parameters.

Wavelength: We introduce the *periodicity length*, Λ, as the distance traveled by the belt between the formation of two subsequent loops, and in the case of meandering, between two subsequent peaks (see Fig. 1B for definition on each of the patterns). Compared to the wavelength, λ, of the pattern, $\Lambda = \lambda$ for meandering, stretched coiling, and translated coiling, and $\Lambda = \lambda/2$ for the alternating loops. In Fig. 4A, we plot Λ versus the dimensionless speed mismatch, along two directions of the parameter sweep: (i) $\epsilon = 0 \rightarrow 1$ (open symbols) and (ii) $\epsilon = 1 \rightarrow 0$ (filled symbols). For (i), the data is well described empirically by,

$$\bar{\Lambda} = \bar{\Lambda}_0(1 - \epsilon^2), \tag{2}$$

where $\bar{\Lambda}_0$ is a constant set by the physical and control parameters. Fitting the data in Fig. 4A to Eq. (2) yields $\bar{\Lambda}_0 = 9.11 \pm 0.15$, which is strikingly similar to the onset meandering wavelength, $\bar{\lambda}_0 \approx 10.5$, of the meandering patterns [27]. In the opposite sweep direction, $\epsilon = 1 \rightarrow 0$, the data still follows Eq. (2) for translated coiling and a portion of the alternating loops, but significantly deviates from it in the regions of bistability; (I,II) and (I,III) in Fig. 2. We have not yet been able to rationalize this discrepancy between the forward and reverse directions of the ϵ sweep.

For a fixed deployment height, we found that $\bar{\Lambda}_0$ is independent of L_{gb} ($\bar{\Lambda}_0 = 9.12 \pm 0.01$ is constant in Fig. 4B, for $\bar{H} = 15$), *i.e.* the dimensional periodicity length of the pattern scales linearly with the gravito-bending length. Moreover, when fixing L_{gb}, we found that $\bar{\Lambda}_0 \sim \log(\bar{H})$, such that $\bar{\Lambda}_0$ depends weakly on $\bar{H}$: $6.6 < \bar{\Lambda}_0 < 11.7$ for a variation of the deployment height in the range $3 < \bar{H} < 238$ for a rod with $L_{gb} = 3.3$ cm (see Fig. S1A).

Loop radius: All coiling patterns other than the meanders, form loops where the rod is deployed over an existing segment already on the belt. Self-contact is not taken into account in our simulations, but this was found to be unimportant in the detailed comparison against experiments [27].

We now introduce the characteristic *loop radius*, $R_o = P/(2\pi)$, where P is the perimeter of the loop. In Fig. 4D, we plot the normalized loop radius, $\bar{R}_o$, versus ϵ (fixing $\bar{H} = 15$). For the alternating loops (triangles) and translated coils (squares), we find the linear variation

$$\bar{R}_o(\epsilon) = \frac{\bar{R}_i(1 - \epsilon_i) + (\epsilon - \epsilon_i)\bar{R}_C}{1 - \epsilon_i}, \tag{3}$$

where $\epsilon_i = 0.37$ is the dimensionless speed mismatch at the onset of the transition between meandering and alternating loops, $\bar{R}_i = \bar{R}_o(\epsilon_i)$ is the normalized radius of the loops at this onset and $\bar{R}_C$ is the normalized *static coiling radius* (deployment onto a static belt [27]) when $\epsilon = 1$. The fit of Eq. (3) to the data is shown as the dashed line Fig. 4D with $\bar{R}_C = 2.02 \pm 0.02$, and $\bar{R}_i = 1.06 \pm 0.02$. However, for the stretched coiling patterns (Fig. 4D, filled circles), there is a significant variation from Eq. (3), which

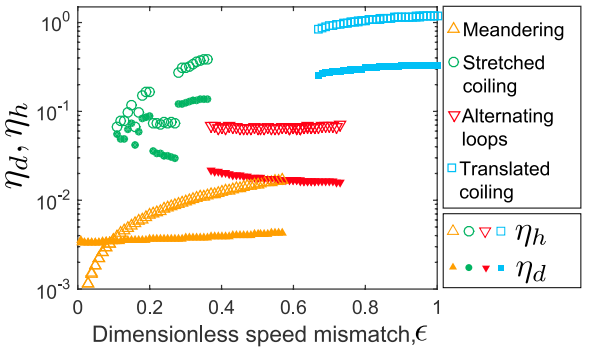

Fig. 5. The twisting to bending energy ratio in the deposited rod, η_d, and in the heel, η_h, for the various patterns, as functions of the dimensionless speed mismatch, ϵ.

we have not yet been able to rationalize. We recall that the stretched coiling patterns are only observed in the reverse sweep direction, $\epsilon = 1 \rightarrow 0$, in a region of bistability of the phase diagram.

Similarly to our characterization of $\bar{\Lambda}$, we now inquire how the loop radius is set by L_{gb} and $\bar{H}$. In Fig. 4E, we plot $\bar{R}_C$ and $\bar{R}_i$ as functions of L_{gb} (fixing $\bar{H} = 15$) and observe that they are both nearly constant at $\bar{R}_C = 2.02 \pm 0.00$, and $\bar{R}_0 = 1.01 \pm 0.01$. The loop radius is therefore set by the gravito-bending length. Both $\bar{R}_C$ and $\bar{R}_i$ do exhibit, however, a logarithmic dependence on $\bar{H}$, that is reminiscent of the above behavior for the heel radius and the wavelength. A more detailed account on how $\bar{R}_C$ and $\bar{R}_i$ depend on $\bar{H}$ is provided in the SI.

7. Interplay between bending and twist

We now turn to evaluating the relative importance of the stored bending and twisting energies, in both the suspended heel and the portion of the rod that is deposited on the belt, beyond the contact point. Given the periodicity of the coiling patterns, it suffices to focus on the strains and energies per unit length for a single wavelength.

We have assumed that the rod is made of an isotropic and linearly elastic material with a Poisson's ratio of $\nu = 0.5$. As such, the ratio of shear and Young's moduli is $G/E = 3$ and the ratio between twisting and bending energies reduces to

$$\eta(s) = \frac{\int_0^s \mathcal{E}_t ds^*}{\int_0^s \mathcal{E}_b ds^*} = \frac{1}{3}\frac{\int_0^s \theta'(s^*)^2 ds^*}{\int_0^s \kappa(s^*)^2 ds^*}. \quad (4)$$

The strains in the deposited rod and in the suspended heel are referred to as (θ_d', κ_d) and (θ_h', κ_h), respectively. The corresponding ratios of twisting to bending energies averaged over a single period of the pattern, are η_d and η_h, respectively (see SI for a non-averaged description, along the arc-length). For the deposited rod on the belt, η_d can be readily calculated from Eq. (4) by integrating over one wavelength beyond αL_{gb} (see Section 3) from the contact point, and the process is averaged over at least 1000 oscillations. For the suspended heel, the integration to obtain η_h is done over the time that it takes to produce a single period of the pattern on the belt (again the process is averaged over at least 1000 oscillations). Realizing that each point s on the deposited rod was deployed at time $t(s)$, the twisting strain in the heel associated with the same s on the deposited loop is $\theta_h' = [\int_h |\theta'(s^*)|ds^*]/h(t)$, where $h(t)$ is the total arc-length of the heel. Similarly, the bending strain is $\kappa_h(s) = [\int_h \kappa(s^*)ds^*]/h(t)$. Substitution of θ_h' and $\kappa_h(s)$ into Eq. (4) yields η_h.

In Fig. 5, we plot the period-averaged twisting to bending ratios, η_d (filled symbols) and η_h (open symbols), as a function of the dimensionless speed mismatch, ϵ. In Fig. 4, we found a smooth variation of the various characteristic lengths ($\bar{\Lambda}$ and $\bar{R}_o$) over the full range of ϵ. By contrast, both η_d and η_h exhibit significant discontinuities at the phase boundaries. The meanders and alternating loops (with $\eta_h, \eta_d \lesssim 0.01$ and $\eta_h, \eta_d \lesssim 0.1$, respectively) are dominated by bending, whereas twist prevails for the translated coils (especially in the suspended heel, where $\eta_h \sim 1$). This behavior can be understood by recognizing that each loop induces a 2π amount of total twist in the rod, while deploying along a straight line releases stored twist by rolling about the centerline. The latter twist removal mechanism is energetically costly for a rod deployed into a curved configuration.

The total accumulated twist is negligible in the meandering mode since no coils form; the build up of twist in the first quarter of the oscillation is released during the second quarter and similarly for the third and fourth quarters, in the opposite direction. Translated coiling comprises primarily circular loops (all in the same coiling direction) resulting in a dominance of twist. For the alternating loops, twist builds during the first half of a period but is then released in the second half by the subsequent loop (symmetric about the x-axis), both separated by an intermediate portion of nearly straight deployment. The stretched coils are an intermediate case ($0.03 < \eta_d < 0.14$ and $0.07 < \eta_h < 0.39$), which was to be expected since these patterns can be interpreted as a juxtaposition of a coiled loop (usually in the same direction) and a portion of a sinusoidal meander (Fig. 1B,II). Interestingly, stretched coiling can be separated into two regions with different values of the twist to bending ratio. When the stretched coils are in the same direction, they follow energy branches that appear to be extensions of those for translated coiling, also with high values of the twist to bending ratios; $\eta_d, \eta_h \gtrsim 0.1$. By contrast, when the stretched coils form on alternate sides, these ratios are significantly lower, $\eta_d, \eta_h \lesssim 0.1$, in what appears to be a continuation of the branches for alternating loops. In spite of this, our motivation to still consider the stretched coiling patterns in a pattern classification of its own is motivated by the analogous stretched coiling patterns of the FMSM [21], which were found to have a uniquely identifying frequency content when compared to all other patterns.

Overall, the twisting to bending energy ratio is larger for the suspended heel than for the deposited pattern. This is presumably due to the fact that self-weight forces the heel to be nearly straight [33], with small $\kappa(s)$, except near the contact point, which does not however affect twist accumulation.

8. Discussion and conclusion

We have quantitatively described the various coiling patterns that form when a thin rod is deployed onto a moving substrate. Our findings emphasize the prominence of the gravito-bending length, L_{gb}, in setting the various length scales of the patterns, which are only modified logarithmically by the deployment height, H. The shape of the suspended heel is also set by L_{gb}. The curvature near its contact point, together with the dimensionless speed mismatch between the injector and the belt, dictate the characteristics of the patterns. The importance of bending in this process was further highlighted by our evaluation of the ratio between twisting to bending energies in the rod. Our characterization in dimensionless form, provides a general predictive account of this pattern formation process. At places, we had to follow an empirical approach, such as in the fits to Eqs. (1)–(3). Given the strongly nonlinear geometry of the problem, rationalizing these findings through analytical methods would have been a challenging endeavor, but we hope that our work will inspire further theoretical efforts in this direction.

Note that we have focused on straight rods, neglecting the effect of natural (i.e. intrinsic) curvature. In practical applications, natural curvature can arise from the storage of cables/pines in spools and can fundamentally alter the coiling behavior, as recently shown for the cases of static coiling and meandering in the ESM [27]. The DER tool that we have used in this study can simulate rods of arbitrary natural configuration, and the common prominence of natural curvature in engineered rodlike structures calls for a similar systematic study on the effect of natural curvature on pattern formation. This is however beyond the scope of the current study and we leave this for future work.

Our results on the ESM call for a direct comparison with the phase diagrams of the patterns that were recently reported for the FMSM [21,23], to which our system shows a remarkable qualitative resemblance. These similitudes are despite the differences in the constitutive descriptions between a viscous thread and an elastic rod. A combined rationalization of these two systems could potentially yield unprecedented design guidelines in a number of engineering processes that have analogous geometries, *e.g.* 3D-printing [3], electrospinning of polystyrene fibers [2] and stretchable electronics components [4].

Acknowledgments

The authors wish to thank Eitan Grinspun and Fang Da for their help with the original numerical simulations, and Pierre-Thomas Brun for enlightening discussion. We are grateful for financial support from the National Science Foundation (CMMI-1129894).

Appendix A. Supplementary data

Supplementary material related to this article can be found online at http://dx.doi.org/10.1016/j.eml.2014.12.004.

References

[1] N. Geblinger, A. Ismach, E. Joselevich, Nat. Nanotechnol. 3 (2008) 195–200.
[2] Y. Xin, D.H. Reneker, Polymer 53 (2012) 4254–4261.
[3] J.A. Lewis, J.E. Smay, J. Stuecker, J. Cesarano, J. Am. Ceram. Soc. 89 (2006) 3599–3609.
[4] R. Carta, P. Jourand, B. Hermans, J. Thoné, D. Brosteaux, T. Vervust, F. Bossuyt, F. Axisa, J. Vanfleteren, R. Puers, Sensors Actuators A 156 (2009) 79–87.
[5] B.C. Gerwick, Construction of Offshore Structures, Wiley, New York, 1987.
[6] S. Chiu-Webster, J. Lister, J. Fluid Mech. 569 (2006) 89–111.
[7] J. Cruickshank, B. Munson, J. Fluid Mech. 113 (1981) 221–239.
[8] L. Mahadevan, W.S. Ryu, A.D. Samuel, Nature 392 (1998) 140.
[9] L. Mahadevan, W.S. Ryu, A.D. Samuel, Nature 403 (2000) 502.
[10] M. Maleki, M. Habibi, R. Golestanian, N. Ribe, D. Bonn, Phys. Rev. Lett. 93 (2004) 214502.
[11] B. Tchavdarov, A. Yarin, S. Radev, J. Fluid Mech. 253 (1993) 593–615.
[12] J. Cruickshank, J. Fluid Mech. 193 (1988) 111–127.
[13] N.M. Ribe, Philos. Trans. R. Soc. Lond. Ser. A Math. Phys. Eng. Sci 460 (2004) 3223–3239.
[14] N.M. Ribe, H.E. Huppert, M.A. Hallworth, M. Habibi, D. Bonn, J. Fluid Mech. 555 (2006) 275–297.
[15] N.M. Ribe, J.R. Lister, S. Chiu-Webster, Phys. Fluids 18 (2006) 124105.
[16] S.W. Morris, J.H. Dawes, N.M. Ribe, J.R. Lister, Phys. Rev. E 77 (2008) 066218.
[17] R.L. Welch, B. Szeto, S.W. Morris, Phys. Rev. E 85 (2012) 066209.
[18] M. Bergou, B. Audoly, E. Vouga, M. Wardetzky, E. Grinspun, ACM Trans. Graph. 29 (2010) 116.
[19] B. Audoly, N. Clauvelin, P.-T. Brun, M. Bergou, E. Grinspun, M. Wardetzky, J. Comput. Phys. 253 (2013) 18–49.
[20] A. Bobenko, J. Sullivan, P. Schröder, G. Ziegler, Discrete Differential Geometry, in: Oberwolfach Seminars, vol. 38, Birkhäuser, Basel, 2008.
[21] P.-T. Brun, N.M. Ribe, B. Audoly, Phys. Fluids 24 (2012) 043102.
[22] G. Barnes, R. Woodcock, Amer. J. Phys. 26 (1958) 205–209.
[23] P.-T. Brun, B. Audoly, N.M. Ribe, T.S. Eaves, J.R. Lister, 2014. arXiv:1410.5382.
[24] L. Mahadevan, J.B. Keller, Philos. Trans. R. Soc. Lond. Ser. A Math. Phys. Eng. Sci. 452 (1996) 1679–1694.
[25] M. Habibi, N. Ribe, D. Bonn, Phys. Rev. Lett. 99 (2007) 154302.
[26] M. Habibi, J. Najafi, N.M. Ribe, Phys. Rev. E 84 (2011) 016219.
[27] M.K. Jawed, F. Da, J. Joo, E. Grinspun, P.M. Reis, Proc. Natl. Acad. Sci. USA 111 (2014) 14663–14668.
[28] M. Bergou, M. Wardetzky, S. Robinson, B. Audoly, E. Grinspun, ACM Trans. Graph. 27 (2008) 63.
[29] F. Peirce, J. Text. Inst. 21 (1930) T377–T416.
[30] M.K. Jawed, F. Da, J. Joo, E. Grinspun, P.M. Reis, Numerical simulation source code, 2014.
URL: http://www.cs.columbia.edu/cg/elastic_coiling/.
[31] B. Audoly, Y. Pomeau, Elasticity and Geometry, Oxford Univ. Press, 2010.
[32] G. Kirchhoff, J. Reine Angew. Math. 56 (1859) 285–313.
[33] J.T. Miller, A. Lazarus, B. Audoly, P.M. Reis, Phys. Rev. Lett. 112 (2014) 068103.